Chemical Engineering Journal 499 (2024) 156295

Contents lists available at ScienceDirect

Chemical Engineering Journal

journal homepage: www.elsevier.com/locate/cej

Modified structure of vanadium oxide *via* cadmium doping and *in-situ* activation for high-performance aqueous zinc ion storage

Ting Chen [a,b], Qianhui Wu [b], Leiming Lang [b,*], Zhidong Chen [c,*], Guoqiang Luo [d], Linfeng Hu [e], Guangxiang Liu [b], Wenshu Chen [e,*]

[a] *School of Materials Science and Engineering, Changzhou University, Changzhou, Jiangsu 213164, PR China*
[b] *Jiangsu Key Laboratory of Zero-Carbon Energy Development and System Integration, Nanjing Xiaozhuang University, Nanjing, Jiangsu 211171, PR China*
[c] *School of Petrochemical Engineering, Changzhou University, Changzhou, Jiangsu 213164, PR China*
[d] *State Key Lab of Advanced Technology for Materials Synthesis and Processing, Wuhan University of Technology, Wuhan 430070, PR China*
[e] *School of Materials Science and Engineering, Southeast University, Nanjing 211189, PR China*

ARTICLE INFO

Keywords:
Vanadium oxide
Structure modification
Cadmium doping
In-situ activation
Aqueous zinc-ion batteries

ABSTRACT

Vanadium oxides are promising cathode materials for aqueous zinc-ion batteries, but they suffer from severe crystal collapse and poor electrical/ionic conductivity. Herein, we successfully synthesized the designed cadmium-doped, carbon-coated vanadium oxide precursor with abundant oxygen vacancies ($Cd_{0.015}V_2O_{3\text{-}x}$@C) using a straightforward one-pot thermal reduction method, followed by *in-situ* activation to form a high-performance cathode material, $Cd_{0.004}V_2O_{5\text{-}y}\cdot nH_2O$@C. We find that the interlayered water dramatically reduces the electrostatic force between zinc ions and $V_2O_{5\text{-}y}$ layers, meanwhile, abundant oxygen vacancies and cadmium doping alter the material's band structure, resulting in enhanced electronic and ionic conductivities. Leveraging these advantages, the phase transitioned $Cd_{0.004}V_2O_{5\text{-}y}\cdot nH_2O$@C cathode delivers a remarkably high capacity of 420 mAh/g (0.2 A/g), an excellent rate capability of 198 mAh/g (20.0 A/g), and an outstanding capacity retention of 78.5 % after 3500 cycles (20 A/g). This synergistic structure modification strategy of elemental doping and *in-situ* activation offers a novel approach to design high-performance vanadium oxide-based cathodes for advanced aqueous batteries.

1. Introduction

Currently, due to the goals for carbon peaking and carbon neutrality, there is an urgent need to develop sustainable energy storage devices suitable for large-scale deployment [1,2]. Lithium-ion batteries have been the cornerstone of energy storage, particularly for portable and automotive applications, but their safety concerns, environmental impact, and high costs call for alternative solutions [3,4]. Aqueous zinc-ion batteries (AZIBs) are gaining significant attention due to their high safety properties, low cost, high theoretical capacity of 820 mAh/g of Zn anode within, a low redox potential of 0.762 V *vs.* SHE, and superior ionic conductivity of aqueous electrolytes, which promises high rate performance [5,6]. However, during the insertion process of divalent zinc ions, challenges such as slow reaction kinetics and host structure collapse arise due to the large hydration radius of zinc ions and strong interactions between zinc ions and host lattice [7]. Consequently, identifying a suitable cathode material with high capacity, fast reaction kinetics, and desirable stability has become one of the keys to enhancing the overall performance of AZIBs.

To date, numerous advanced cathode materials have been explored for aqueous zinc-ion batteries, including manganese-based compounds [8–10], vanadium-based compounds [11,12], Prussian blue analogues [13,14], and conductive polymers [15,16]. Vanadium-based compounds, in particular, have emerged as potential cathodes due to their layered/tunnel structures, low cost, and low toxicity. However, the strong electrostatic interactions between the divalent Zn^{2+} ions and vanadium oxides (VO_x), coupled with the poor conductivity of the cathodes and irreversible structural damage during cycling, often lead to significant capacity fading [17–19].

To tackle the aforementioned issues of VO_x, researchers have employed several strategies to enhance their electrochemical performance. Introducing oxygen vacancies/defects is a common modification

---

* Corresponding authors at: Jiangsu Key Laboratory of Zero-Carbon Energy Development and System Integration, Nanjing Xiaozhuang University, Nanjing, Jiangsu 211171, PR China (L. Lang).

E-mail addresses: langleiming@njxzc.edu.cn (L. Lang), chenzd@cczu.edu.cn (Z. Chen), 101013800@seu.edu.cn (W. Chen).

https://doi.org/10.1016/j.cej.2024.156295
Received 27 June 2024; Received in revised form 30 August 2024; Accepted 29 September 2024

strategy. On one hand, the creation of oxygen vacancies generates additional voids in the lattice structure, which act as channels for zinc ion migration, thus accelerating zinc ion diffusion. On the other hand, oxygen vacancies alter the electronic structure of the lattice, creating more electronic defect states that serve as pathways for electron conduction, thereby improving the material's electronic conductivity [20–24]. Carbon/organic polymer coating is also an effective strategy to enhance vanadium-based cathodes. It not only improves the inherent poor conductivity of vanadium-based cathodes but also, through appropriate interface engineering (such as core–shell structures and heterojunction formation), can mitigate stress deformation during cycling [25–27]. Further, the insertion of cations, polymers, or water molecules into the layered vanadium oxides, for instance of $(Zn_{0.1}, Ch_{0.1})V_2O_{4.92}\cdot 0.56H_2O$ [28],$Ag_{0.4}V_2O_5$ [29], $Al_{0.15}V_2O_5\cdot 1.01H_2O$ [30], $Ba_{0.26}V_2O_5\cdot 0.92H_2O$ [31], $Ca_{0.23}V_2O_5\cdot 0.95H_2O$ [32] and $K_2V_6O_{16}\cdot 1.5H_2O$ [33], has also been adopted to improves the ion diffusion capabilities *via* pillar effects, thereby enhancing the electrochemical reaction kinetics and cycling stability. Despite the use of various performance improvement strategies mentioned above, the overall performance of VO_x remains unsatisfactory. There is still a lack of a method that can simultaneously improve the density of active sites, structural stability, and electronic/ionic conductivity of VO_x to synergistically enhance its capacity, rate capability, and cycling stability.

In this work, we propose a structure modification strategy of carbon layer coating along with cadmium doping followed by *in-situ* electrochemical activation to address the mentioned issues for vanadium oxides. We first prepared a carbon-coated and cadmium-doped vanadium oxide of $Cd_{0.015}V_2O_{3-x}$@C (denoted as $CdVO_x$@C) through a straightforward high-temperature thermal reduction approach, and then converted it into a water-intercalated and oxygen vacancy-abundant V_2O_5 type cathode of $Cd_{0.004}V_2O_{5-y}\cdot nH_2O$@C (denoted as $CdHVO_y$@C) *via* an *in-situ* electrochemical activation process. We find that the phase transitioned $CdHVO_y$@C remains the pre-doped cadmium and abundant oxygen vacancies, which can effectively increase the density of active sites for zinc ion storage, enhance the electrical conductivity of the cathode and decrease the migration energy barrier of Zn^{2+}. Additionally, the introduced water molecules inside the $CdHVO_y$@C can act as "lubricants" to decrease the strong electrostatic repulsion force between VO layers. Benefit from these advantages, the activated $Cd_{0.004}V_2O_{5-y}\cdot nH_2O$@C cathode exhibits a remarkably high capacity of 420 mAh/g at 0.2 A/g, an excellent rate capability of 198 mAh/g at 20 A/g, and an outperforming capacity retention of 78.5 % after 3500 cycles at 20 A/g. This work offers a novel and simple approach to prepare high-performance vanadium oxide-based cathode materials for sustainable AZIBs.

2. Results and discussion

To visually represent the synthesis and *in-situ* electrochemical activation process for obtaining the desired $CdHVO_y$@C cathode material, a schematic is illustrated in Scheme 1. Initially, glucose and hydrogen peroxide are utilized as reducing agents to convert V^{5+} into V^{3+}. Then, we use a high-temperature calcination method under an inert atmosphere to simultaneously dope the Cd element into the VO_x crystal, and form carbon coating layers onto the VO_x. This process yields a precursor of $CdVO_x$@C. Subsequently, the *in-situ* electrochemical activation process leads to the oxidation of V^{3+} to V^{5+} and phase transition, resulting in the formation of the high-performance AZIBs cathode of $CdHVO_y$@C. This process, in which low-valence vanadium oxides undergo an irreversible phase transition, transforming into V_2O_5-type compounds upon *in-situ* activation at voltages exceeding 1.6 V (*vs.* Zn/Zn^{2+}), has been reported in some recent studies [34–37]. We also adjusted variables such as cadmium doping levels and calcination temperature to optimize the preparation conditions (Fig. S1). We therefore anticipate to prepare a desirable cathode through this simple and effective electrochemical activation method, which can adaptively regulate the material's structure and is expected to enhance the zinc ion storage performance.

X-ray diffraction (XRD) with Rietveld refinement was utilized to derive the crystallographic details of the samples. Fig. 1a illustrates a satisfactory Rietveld refinement plot for $CdVO_x$@C, with an acceptable weighted profile R factor ($R_{wp} = 3.1$ %). The crystal structure is indexed to the rhombohedral *R-3c* space group with lattice parameters of $a = b = 4.95004$ Å, $c = 13.9984$ Å, $\alpha = \beta = 90^\circ$, $\gamma = 120^\circ$, and a unit cell volume of V=297.048 $Å^3$ (Table S1), corresponding to the V_2O_3 phase (PDF# 97–020-1107). The refinement result suggests a propensity for Cd to replace V atoms in the V_2O_3 lattice. Based on the ICP analysis, we

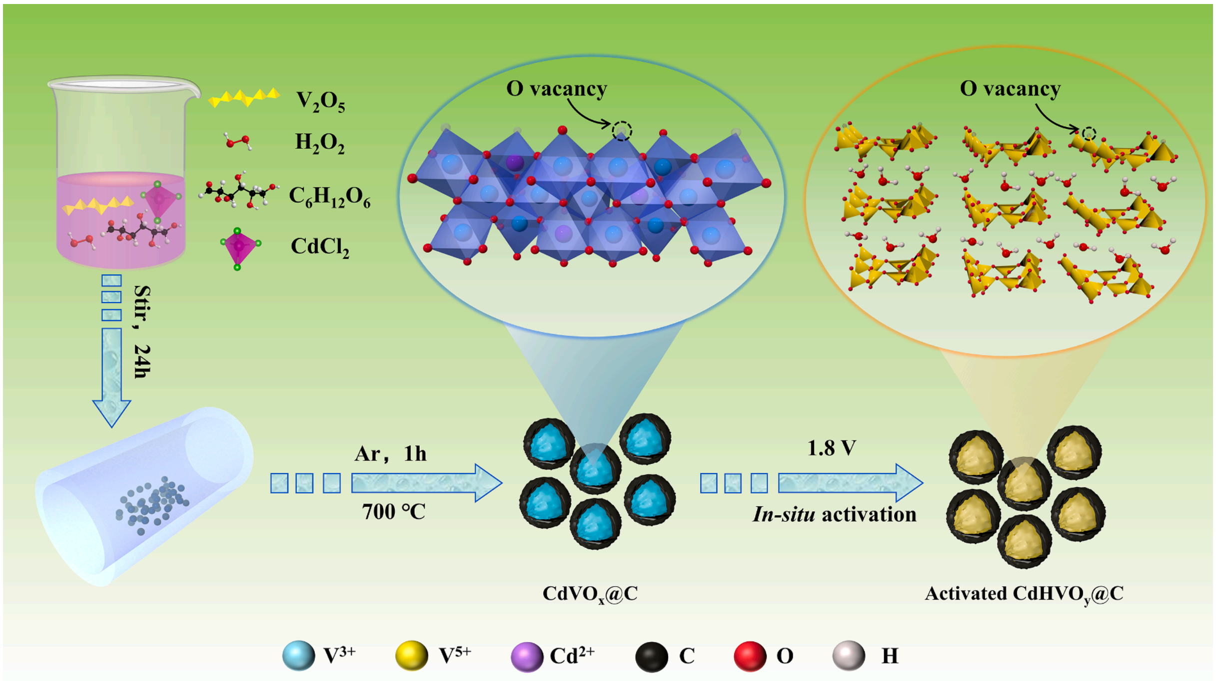

Scheme 1. A schematic of the preparation and *in-situ* electrochemical activation process for $CdHVO_y$@C.

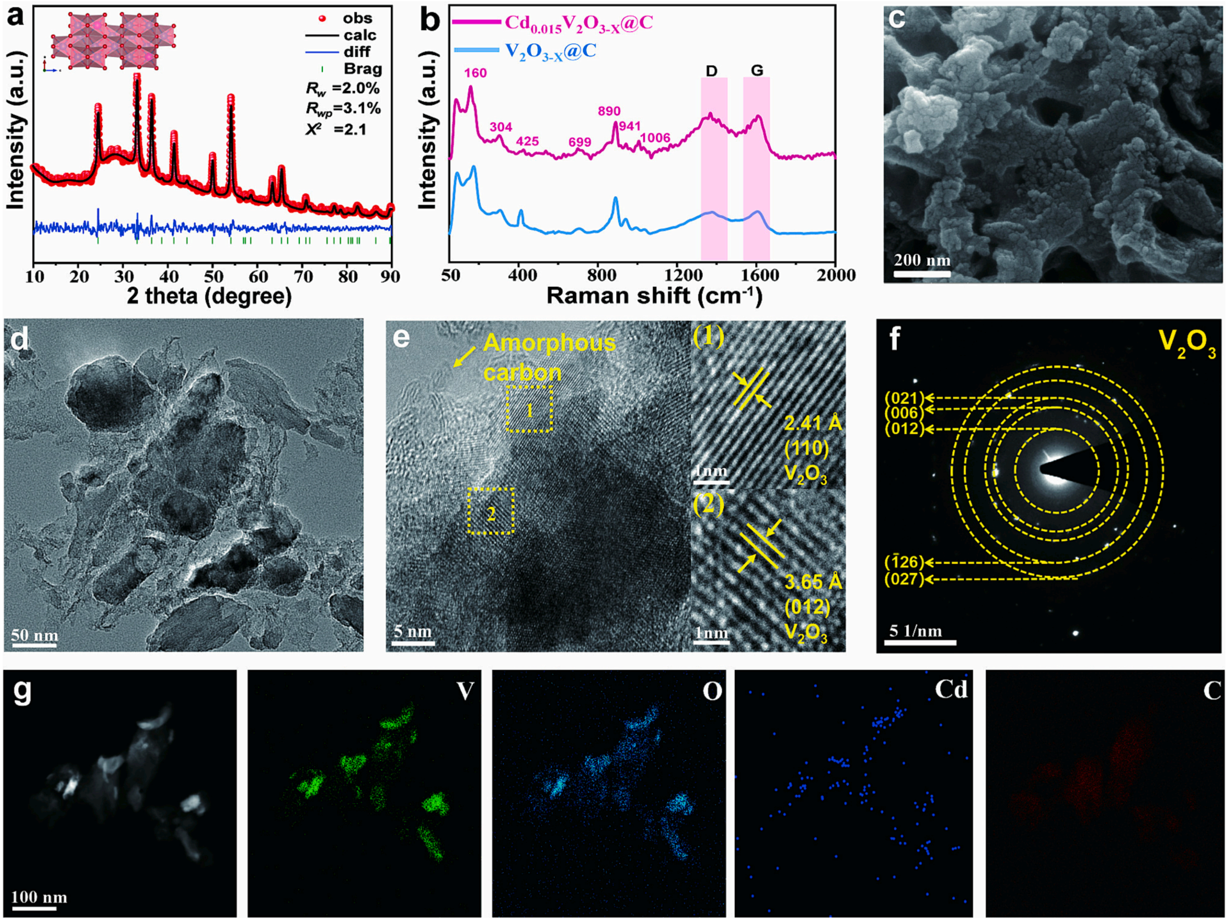

Fig.1. (a) XRD pattern with Rietveld refinement of CdVO$_x$@C. (b) Raman spectra of VO$_x$@C and CdVO$_x$@C. (c) SEM image, (d) TEM image, (e) HRTEM image, (f) SAED pattern and (g) HAADF-STEM image and EDS mappings results of CdVO$_x$@C.

identify the specific chemical formula of the doping product to be Cd$_{0.015}$V$_2$O$_{3-x}$@C (Table S2). Raman signals observed between 100 and 1100 cm^{-1} originate from the crystalline structure of V$_2$O$_3$ (Fig. 1b), which is consistent with XRD results. Specifically, peaks at 160, 304, 425, and 699 cm^{-1} are attributed to the vibrational modes of V–O bonds and the peak at 1006 cm^{-1} belongs to the V=O bond in vanadium oxides [38]. The Raman spectra of CdVO$_x$ also exhibit the D band (~1367 cm^{-1}) and G band (~1610 cm^{-1}), which are indicative scattering signals of disordered and graphitic carbon structures, respectively (Fig. S2). The height intensity ratios of D to G bands (I_D/I_G) for CdVOx@C and VOx@C are 3.09 and 4.17, respectively, suggesting that the doped sample of CdVO$_x$@C possesses a reduced degree of amorphous/defective carbon [39]. According to thermogravimetric analysis (TGA, Fig. S3), the weight ratio of carbon content in the CdVO$_x$@C composite is about 15.8 %.

The morphology of the prepared CdVO$_x$@C was further characterized using scanning electron microscopy (SEM) and transmission electron microscopy (TEM) (Fig. 1c-g). Unlike the flake-petal morphology of VO$_x$@C, the morphology of CdVO$_x$@C changes upon the incorporation of cadmium, where the surface consists of microspheres within diameters of approximately 30 – 40 nm that aggregate and form numerous pores (Fig. 1c, S4). The specific surface area was measured and results show that CdVO$_x$ has a much larger specific surface area of 85.6 m^2/g compared to 8.5 m^2/g for VO$_x$ (Fig. S5). We speculate that this phenomenon may be caused by the volatilization of cadmium chloride in the raw material under high-temperature conditions, bringing a gas-phase reaction that affects the microstructure of the CdVO$_x$@C. The increased specific surface area not only facilitates the penetration of the electrolyte and reduces the ion diffusion path, but also provides more active sites for electrochemical reactions, thereby improving the performance of the cathode [20]. Amorphous carbon coating layer can be identified on the surface of CdVO$_x$@C from the TEM observations (Fig. 1 d and e). The high-resolution TEM (HRTEM) image shows the high crystallinity feature for CdVO$_x$@C. The lattice spacings of 2.41 and 3.65 Å in the highlighted regions within the yellow frames (marked as 1 and 2) correspond to the *d* spacings of (1 1 0) and (0 1 2) planes for hexagonal V$_2$O$_3$, respectively. The rings in the selected area electron diffraction (SAED) pattern originate from various crystal planes of the V$_2$O$_3$ phase, which further confirms the polycrystalline property of CdVO$_x$@C (Fig. 1f). The TEM coupled energy dispersive X-ray spectroscopy (EDX) elemental mapping images (Fig. 1g) indicate a uniform distribution of vanadium, oxygen, carbon, and cadmium elements in CdVO$_x$@C.

To gain a deeper understanding of the chemical and structural properties of VO$_x$@C and CdVO$_x$@C, X-ray photoelectron spectroscopy (XPS) analyses were conducted. The successful doping of cadmium in the CdVO$_x$@C sample is confirmed through the survey spectrum, with the Cd 3*d* spectrum exhibiting peaks at 405.8 and 412.4 eV, which are attributed to the Cd 3$d_{5/2}$ and Cd 3$d_{3/2}$ orbitals of Cd^{2+}, respectively (Fig. S6) [40]. As shown in Fig. 2a, the XPS spectra of V 2*p* orbital for both VO$_x$@C and CdVO$_x$@C show two spin–orbit splitting peaks of 2$p_{3/2}$ and 2$p_{1/2}$, with a peak separation of 7.4 eV [35]. These peaks can be deconvoluted into individual components corresponding to V^{3+} and V^{2+} oxidation states [41]. The O 1 *s* spectrum of CdVO$_x$@C, as presented in Fig. 2b, is decomposed into three distinct peaks at binding energies of 530.6, 531.2, and 533.4 eV, which correspond to V–O, oxygen vacancies, and C=O, respectively. The oxygen vacancy proportion in CdVO$_x$@C is determined to be 15.1 %, according to the deconvolution

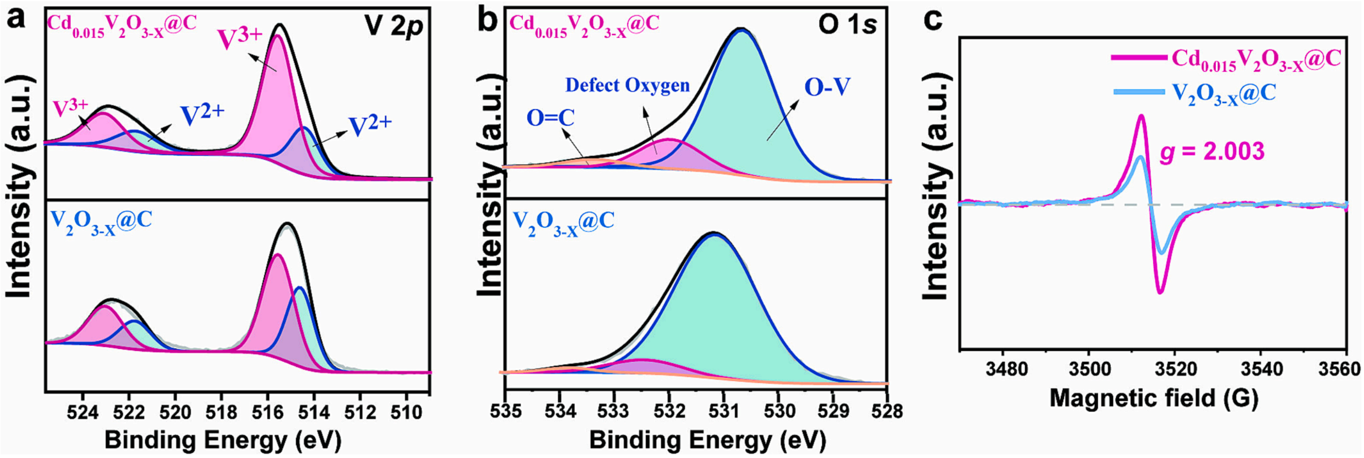

Fig.2. High resolution XPS spectra for (a) V 2*p* and (b) O 1 *s* orbitals of VO_x@C and $CdVO_x$@C. (c) EPR spectra of VO_x@C and $CdVO_x$@C.

results of O 1 *s* XPS data, which is higher than the 7.2 % found in VO_x@C, indicating an increased oxygen vacancies induced by the Cd doping (Table S3). The O 1 *s* peak in VO_x@C shifts to a higher binding energy compared to that of $CdVO_x$@C, which could be attributed to the introduction of cadmium which alters the electron density around the V–O bonds. As cadmium has a lower electronegativity than vanadium, it decreases the electron density of neighboring oxygen atoms, leading to a lower binding energy shift for the O 1 *s* peak [42]. In Fig. 2c, the electron

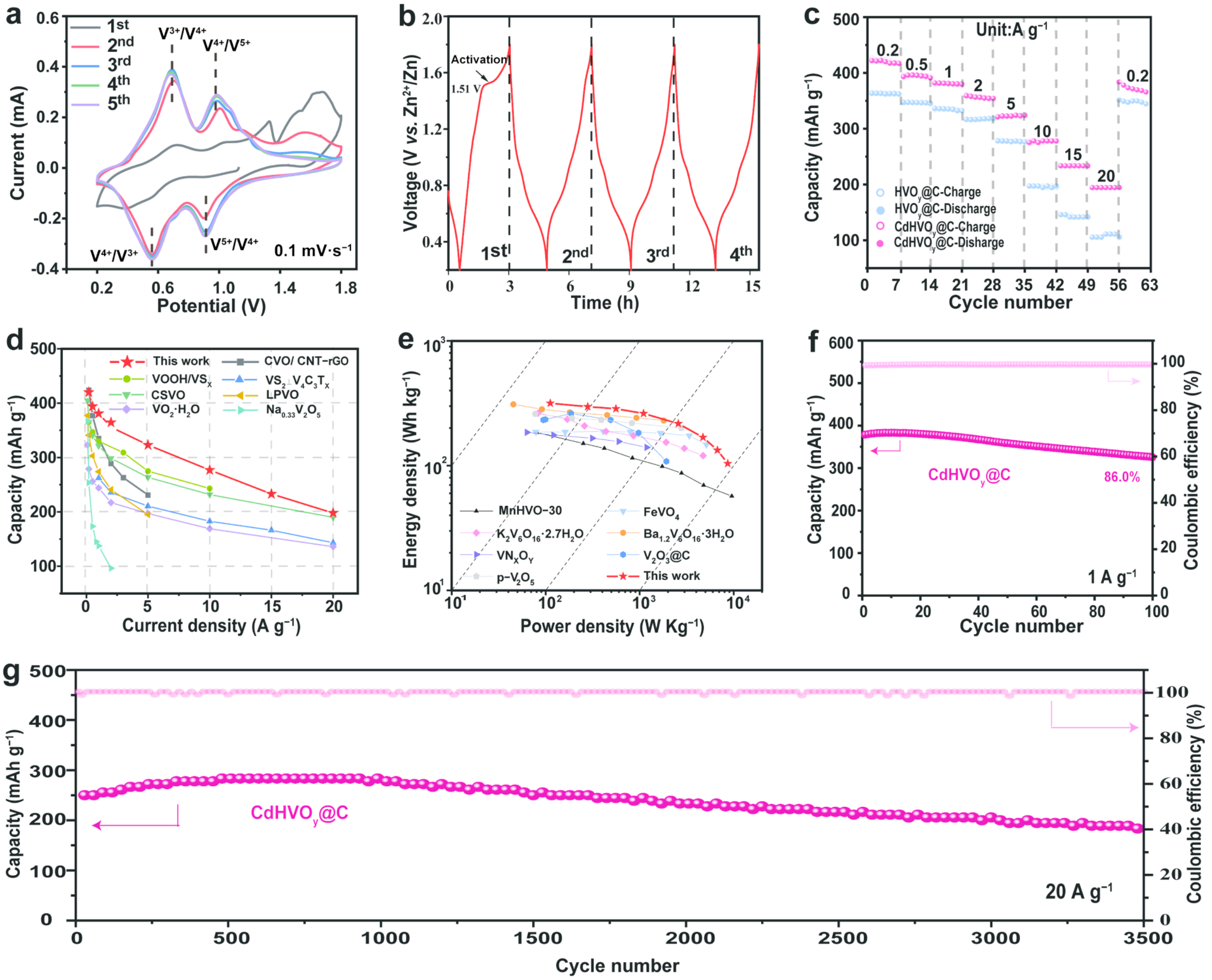

Fig.3. (a) Cyclic voltammetry (CV) curves for the initial five cycles of $CdHVO_y$@C. (b) GCD profiles of $CdHVO_y$@C at 0.2 A/g. (c) Rate performance of CdHVOy@C and HVO_y@C. (d) A comparison of rate performance and (e) Ragone plots of $CdHVO_y$@C and some other recently reported cathode materials. Cycling performance of $CdHVO_y$@C at (f) 1 A/g and (g) 20 A/g.

paramagnetic resonance (EPR) spectra reveal that CdVO$_x$@C exhibits a pronounced symmetric peak with an isotropic g value of 2.003, confirming the abundance of oxygen vacancies. The absence of oxygen atoms results in numerous dangling bonds for neighboring vanadium atoms, which can be stabilized by interactions with other atoms (such as adsorbed H^+/Zn^{2+}), making them electrochemically active and substantially improving the specific capacity. Also, oxygen vacancies create additional pathways for ion migration, reducing the energy barrier for zinc ion diffusion, thereby enhancing the electrochemical ion storage kinetics [35]. It is worth mentioning that while oxygen vacancies can enhance cathode performance, more is not always better; inappropriate structural adjustments can also lead to a decline in performance (Fig. S1, S7).

To validate the advance of our structure modification strategy, we evaluated the electrochemical zinc ion storage performance of CdHVO$_y$@C within a voltage window of 0.2–1.8 V (Fig. 3). The first-cycle cyclic voltammetry (CV) curve of CdHVO$_y$@C at a scan rate of 0.1 mV/s, as depicted in Fig. 3a, exhibits a distinct shape compared to that of the subsequent cycles, with a broad oxidation peak appearing between 1.45 V and 1.7 V, which disappears in later cycles, indicating an irreversible phase transformation where $Cd_{0.0015}V_2O_{3\text{-}x}$@C transforms into $Cd_{0.04}V_2O_{5\text{-}y}\cdot nH_2O$@C (Fig. S8, Table S2). This irreversible phase transformation is generated from an *in-situ* electrochemical activation process in which the structure evolves into a layered V_2O_5-type material, with water molecules intercalated. Two pairs of redox peaks located at 0.56/0.68 V and 0.90/0.98 V suggest a two-step reaction mechanism of zinc ion insertion/extraction [43]. Additionally, the CV curves of the initial three cycles show an increasing trend in the redox peak intensity, which is correlated with the structural evolution caused by the incomplete extraction of Zn^{2+} ions intercalated into the vanadium pentoxide lattice [44]. Fig. 3b shows the initial four GCD cycles, where the first charge curve exhibits a transient voltage plateau at 1.51 V, corresponding to an oxygen evolution reaction (OER) occurring at this voltage [34]. This plateau disappears in subsequent cycles, consistent with the results observed in the CV curves. Notably, the activation time of CdVO$_X$@C during the first cycle was approximately 149 min, shorter than most of the recently reported vanadium-based materials requiring for electrochemical activation at the similar current densities (Table S4), demonstrating that CdVO$_X$@C has the ability for rapid phase transition (activation). We tested the high-resolution XPS spectra of the CdHVO$_y$@C cathode after the 15th cycle, confirming the insertion of water and the presence of oxygen vacancies. The proportion of oxygen vacancies slightly decreases compared to the unactivated CdVO$_x$@C (Fig. S9 and Table S3), which is likely due to the material's adaptive adjustment during the phase transition process.

To assess the effect of oxygen vacancies and cadmium doping on the electrochemical zinc ion storage performance, we further studied the rate performance of CdHVO$_y$@C. Fig. 3c presents the rate capability of CdHVO$_y$@C in comparison with HVO$_y$@C. The reversible specific capacities for CdHVO$_y$@C at various current densities of 0.2, 0.5, 1, 2, 5, 10, 15, and 20 A/g are 420, 394, 381, 356, 323, 277, 233, and 198 mAh/g, respectively, which are higher than those for HVO$_y$@C (Fig. S10). As expected, the rate capability of CdHVO$_y$@C is much better than many recently reported high-performance vanadium-based cathodes, such as $(C_6H_4NH\text{-})_{0.39}Li_{0.68}V_2O_5\cdot 1.69H_2O$ [45]; $Cs_{0.53}V_2O_5\cdot 0\cdot .58H_2O$ [46], $V_2O_5\cdot nH_2O$ [47], $VO_2\cdot xH_2O$ [48], demonstrating the superior zinc ion storage kinetics of CdHVO$_y$@C (Fig. 3d). Fig. 3e depicts the Ragone plot of CdHVO$_y$@C in comparison with some other recently reported vanadium-based cathode materials. Results show that the CdHVOy@C cathode delivers a power density of 316.6 Wh kg^{-1} at an energy density of 111.9 Wh kg^{-1}. Even at a higher power density of 8.6 KW kg^{-1}, it still maintains an energy density of 104.1 W kg^{-1}, surpassing many previously reported vanadium-based cathode materials (Fig. 3e and Table S5) [49–55].

The cycling performance of the activated product of CdHVO$_y$@C was then investigated at various current densities for working stability evaluation. We first performed the cycling test of CdHVO$_y$@C at a current density of 1 A/g (Fig. 3f). Results show that the CdHVO$_y$@C exhibits an impressive capacity retention of 86.0 % (326 mAh/g) after 100 cycles, much higher than the specific capacity of 278 mAh/g for HVO$_y$@C after 100 cycles (Fig. S11). Meanwhile, a marginal increase in specific capacity for CdHVO$_y$@C is observed in the initial cycles, which can be attributed to the material's structural evolution during early electrochemical cycling. Moreover, this activation phenomenon is more pronounced at lower current densities, elucidating the necessity for additional cycles to achieve activation at an elevated current density of 20 A/g for CdHVO$_y$@C [20,35]. To investigate the solubility of vanadium and cadmium in the cathode during cycling, we designed a dual-electrode system to study their solubility at different cycles. The experimental results indicate that CdHVO$_y$@C exhibits significant vanadium and cadmium dissolution during the initial cycles due to material self-adjustment, with dissolution stabilizing in subsequent cycles. Compared to HVO$_y$@C, CdHVO$_y$@C shows less vanadium dissolution, suggesting that cadmium doping inhibits vanadium dissolution in the electrolyte to some extent. We select the doping element of cadmium from the consideration of the following aspects: (i) The relatively larger atomic radius of cadmium (161 pm *vs.* 134 pm of vanadium) may introduce moderate stress in the doped crystal, helping to alleviate internal stress from volume changes during charge–discharge cycles, thus enhancing the structural stability. (ii) The slight electronegativity difference between cadmium (1.69) and vanadium (1.63) leads to a redistribution of the surrounding electron cloud, thereby optimizing the electronic structure. (iii) Cadmium's relatively stable chemical nature can effectively suppress the dissolution and side reactions in aqueous electrolytes. However, capacity decay is influenced by multiple factors, and further efforts are needed to address this issue from various perspectives (Fig S12). We then checked the cycling performance of the electrode at a high current density of 20.0 A/g (Fig. 3g). Under high current, the cathode often requires more cycles for structural evolution, during which capacity may increase to some extent (Fig S13). After full activation, the maximum specific capacity of the CdHVOy@C cathode reaches 283 mA h/g, and after 3500 cycles, it retains a satisfying capacity of 183 mAh/g (78.5 % of its initial capacity), which is higher than the 156 mAh/g of HVO$_y$@C after the same number of cycles (Fig. S14). The GCD curves at various cycles under 20.0 A/g display the typical vanadium-based sloped profiles. As the material stabilizes, the differential capacity curves also exhibit consistent peak shapes, collectively indicating that CdHVOy@C can effectively cycle under high current (Fig S15). SEM images of the cathode at different cycles show that with increased cycling, the cathode gradually breaks down from a bulk structure to finer fragments, with more separator material and byproducts accumulating on the electrode (Fig S16). Based on these results, we conclude that our proposed structure modification strategy of carbon layer coating along with cadmium doping followed by *in-situ* electrochemical activation successfully enhances the zinc ion storage performance of vanadium oxides in capacity and rate capability.

We continue to study the detailed Zn ion storage kinetics in the phase-transformed product of CdHVO$_y$@C to reveal the electrochemical energy storage mechanisms. The solid-state diffusion coefficient (D_{Zn}^{2+}) within the electrodes was assessed using a galvanostatic intermittent titration technique (GITT, Fig. 4a). The estimated D_{Zn}^{2+} of CdHVO$_y$@C spans from 1.6×10^{-10} to 1.5×10^{-11} cm^2 s^{-1} over the entire discharge/charge process. The two distinct stages in the zinc migration coefficient during discharge correspond to H^+ insertion and the slower Zn^{2+} insertion. In comparison, the HVO$_y$@C demonstrates a smaller D_{Zn}^{2+} as displayed in Fig. S17, where D_{Zn}^{2+} fluctuates from 1.4×10^{-10} to 4.1×10^{-12} cm^2 s^{-1}. These results suggest that the CdHVO$_y$@C electrode facilitates more rapid charge transfer kinetics. We then use a CV test to gain further insight into the electrochemical reaction kinetics of CdHVO$_y$@C. Fig. 4b presents the CV curves of CdHVO$_y$@C electrode at scan rates ranging from 0.1 to 1.0 mV/s within a potential window of 0.2 − 1.8 V. As the scan rate increases, the oxidation/reduction peaks

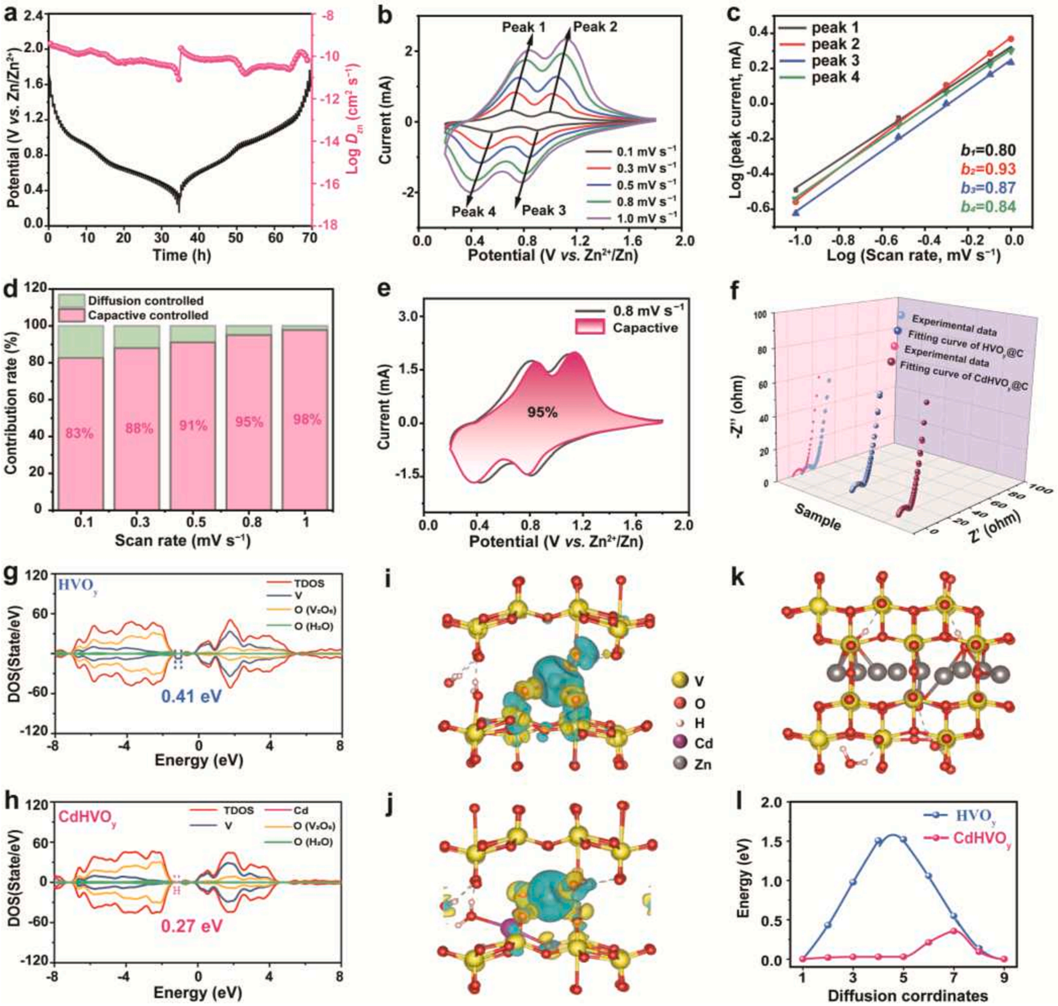

Fig.4. (a) Charge and discharge GITT curves of CdHVO$_y$@C at the current density of 0.2 A/g and the corresponding Zn^{2+} diffusion coefficients. (b) CV curves of the CdHVO$_y$@C at various scan rates and (c) the corresponding plots of log (i) *vs.* log(ν). (d) Capacitance contribution at different sweep rates, (e) CV curves of CdHVO$_y$@C with a calculated capacitance contribution at 0.8 mV/s. (f) Nyquist plots of HVO$_y$@C and CdHVO$_y$@C after 15 cycles at the state of 1.8 V. Density of states for (g) HVO$_y$ and (h) CdHVO$_y$. Charge density with Zn^{2+} intercalation in (i) HVO$_y$ and (j) CdHVO$_y$. The dark yellow and cyan regions represent net electron accumulation and depletion, respectively. (k) Zn^{2+} ion diffusion pathway in CdHVO$_y$. (l) Zn^{2+} ion diffusion energy barriers in HVO$_y$ and CdHVO$_y$.

progressively shift towards more positive/negative potentials. Here, we compare the peak potential separations (ΔV) of CdHVO$_y$@C and HVO$_y$@C at the scan rate of 0.8 mV/s. For CdHVO$_y$@C, the oxidation and reduction peaks are located at 0.799/0.444 V and 1.089/0.812 V, respectively. In contrast, for HVO$_y$@C, the peaks are located at 0.937/0.362 V and 1.247/0.797 V respectively (Fig. S18). The corresponding ΔV for CdHVO$_y$@C are 0.355 V and 0.277 V, which are less than those for HVO$_y$@C (0.575 V and 0.45 V, respectively). This indicates that CdHVO$_y$@C experiences less polarization and faster zinc ion insertion/extraction kinetics.

The contributions to capacity from capacitance- and diffusion-controlled effects can be quantified by the power rate relationship between peak current (i) and scan rate (ν), with the detailed calculation process outlined in the Supporting Information. As shown in Fig. 4c, logarithmic linear fitting of peak currents of 1 to 4 against scan rates yields b values of 0.80, 0.93, 0.87, and 0.84, respectively, for CdHVO$_y$@C. Whereas, the undoped sample of HVO$_y$@C presents b values of 0.70, 0.93, 0.86, and 0.75, respectively (Fig. S19). This suggests that the Zn^{2+} storage processes for both electrodes are governed by a mixed controlling mechanism, predominantly capacitive contribution. The contributions of capacitance-controlled process ($k_1\nu$) and diffusion-controlled processes ($k\ _2\nu^{1/2}$) to the total capacity are calculated and illustrated in Fig. 4d. Results show that for CdHVO$_y$@C, the capacitive contribution increases from 83 % to 98 % as the sweep rate changes from 0.1 to 1.0 mV/s. In comparison, the capacitive contributions of HVO$_y$@C are slightly lower than those of CdHVO$_y$@C (Fig. S20). Fig. 4e illustrates the fitted CV profiles at 0.8mV/s, where the pink region indicates the capacitance-controlled contribution, accounting for a significant ratio of 95 % for CdHVO$_y$@C. The high contribution of pseudo-capacitance facilitates rapid charge storage, endowing the CdHVO$_y$@C electrode with superior rate capability.

Electrochemical impedance spectroscopy (EIS) measurements were conducted to investigate the electrochemical charge/ion transport kinetics of the CdHVO$_y$@C (Fig. 4f). The semicircle in the high-frequency region corresponds to the charge transfer resistance (R_{ct}), and the sloping line in the low-frequency region is associated with the Zn^{2+} diffusion at the electrode–electrolyte interface (Warburg resistance, W_0) [54,56]. As inferred from the fitting results (Table S6 and Fig. S21), the CdHVO$_y$@C exhibits a lower R_{ct} (8.77 Ω) and R_s (3.23 Ω) compared to those of HVOy@C (16.76 Ω and 17.82 Ω), indicating that the CdHVOy@C cathode material possesses faster electrochemical reaction kinetics and higher electrical/ion conductivity, thus ensuring rapid Zn^{2+} insertion/extraction.

The origin of the excellent Zn^{2+} storage performance for the CdHVOy@C cathode was further analyzed from theoretical views using density functional theory (DFT) calculations. As illustrated in Fig. S22, three models were employed: pure vanadium pentoxide (V_2O_5), water-intercalated vanadium pentoxide with oxygen deficiency (HVO_y), and water-intercalated, cadmium-doped vanadium pentoxide with oxygen deficiency ($CdHVO_y$). The density of states (DOS) results reveal that the pure V_2O_5 exhibits the largest bandgap (Fig. S23). The synergistic effect of oxygen vacancies and water molecules significantly reduces the bandgap of HVO_y to 0.41 eV. Furthermore, with a small amount of cadmium replacing vanadium, the bandgap of CdHVOy further decreases to 0.27 eV. The substitution of cadmium alters the electronic structure of the material by increasing the density of electronic states between energy levels. This results in higher energy at the Fermi level, making $CdHVO_y$ a better electrical conductivity (Fig. 4g, h). The calculated differential charge density results (Fig. 4i, j) indicate that cadmium doping in $CdHVO_y$ induces structural distortions, resulting in a larger charge accumulation around cadmium atoms compared to that of HVO_y. Additionally, a bigger charge dissipation region is observed near zinc ions in $CdHVO_y$, suggesting the presence of larger diffusion channels for Zn^{2+}, which will enhance the ion diffusion performance of the electrode. Fig. 4k illustrates the migration pathway of zinc ions in the interlayers of $CdHVO_y$. The Zn^{2+} diffusion barriers in HVO_y and $CdHVO_y$ cathodes are found to be 1.52 eV and 0.36 eV, respectively, further demonstrating the excellent ion diffusion capability of Zn^{2+} in the $CdHVO_y$ cathode (Fig. 4l).

To demonstrate the practical applications of the $CdHVO_y$@C cathode, we assembled Zn//$CdHVO_y$@C pouch cells, with the schematic of flexible AZIBs depicted in Fig. 5a. The open-circuit voltage of two series-connected pouch cells reaches 2.67 V, confirming the successful assembly of the batteries (Fig. 5b). We further conducted flexibility tests on the Zn//$CdHVO_y$@C pouch cell with a cathode loading of 4 mg cm^{-2}, finding that the pouch cell operates stably when folded at angles of 0°, 45°, 90° and 180°. After 20 folding cycles at a current density of 0.5 A/g, it retains a specific capacity of 299 mAh/g (Fig. 5c). Moreover, two $CdHVO_y$@C//Zn pouch cells in series can successfully power LED lights in all bent states, as shown in Fig. 5d-g, demonstrating the unique potential of designed $CdHVO_y$ cathode for flexible AZIB applications.

3. Conclusions

In summary, we have successfully adopted a structure modification strategy of carbon layer coating combined with cadmium doping, followed by *in-situ* electrochemical activation to synthesize a high-performance AZIB cathode material of $CdHVO_y$@C. Characterizations reveal that the activated $CdHVO_y$@C retains the doped cadmium and oxygen vacancies, accompanied by water intercalation. DFT calculations indicate that interlayered water dramatically reduces the electrostatic force between zinc ions and $V_2O_{5\text{-}y}$ layers, while abundant oxygen vacancies and cadmium doping modify the material's band structure, resulting in enhanced electrical conductivity and ion transport properties. The phase-transformed cathode of $CdHVO_y$@C delivers an extraordinarily high specific capacity (420 mAh/g at 0.2 A/g), an outstanding rate capability (198 mAh/g at 20 A/g), and an impressive cycling stability performance (78.5 % retention after 3500 cycles at 20 A/g). This work not only paves the way for preparing advanced vanadium-based cathodes for high-performance AZIBs *via* a simple doping followed by *in-situ* activation process but also may further inspire the development of more electrode materials for efficient energy storage.

CRediT authorship contribution statement

Ting Chen: Writing – review & editing, Writing – original draft, Methodology, Formal analysis, Data curation. **Qianhui Wu:** Formal analysis, Data curation. **Leiming Lang:** Writing – review & editing, Supervision, Investigation, Funding acquisition, Conceptualization. **Zhidong Chen:** Supervision, Investigation, Formal analysis, Conceptualization. **Guoqiang Luo:** Formal analysis, Data curation. **Linfeng Hu:** Formal analysis, Data curation. **Guangxiang Liu:** Formal analysis, Data curation. **Wenshu Chen:** Writing – review & editing, Supervision, Methodology, Investigation, Funding acquisition, Formal analysis, Data curation, Conceptualization.

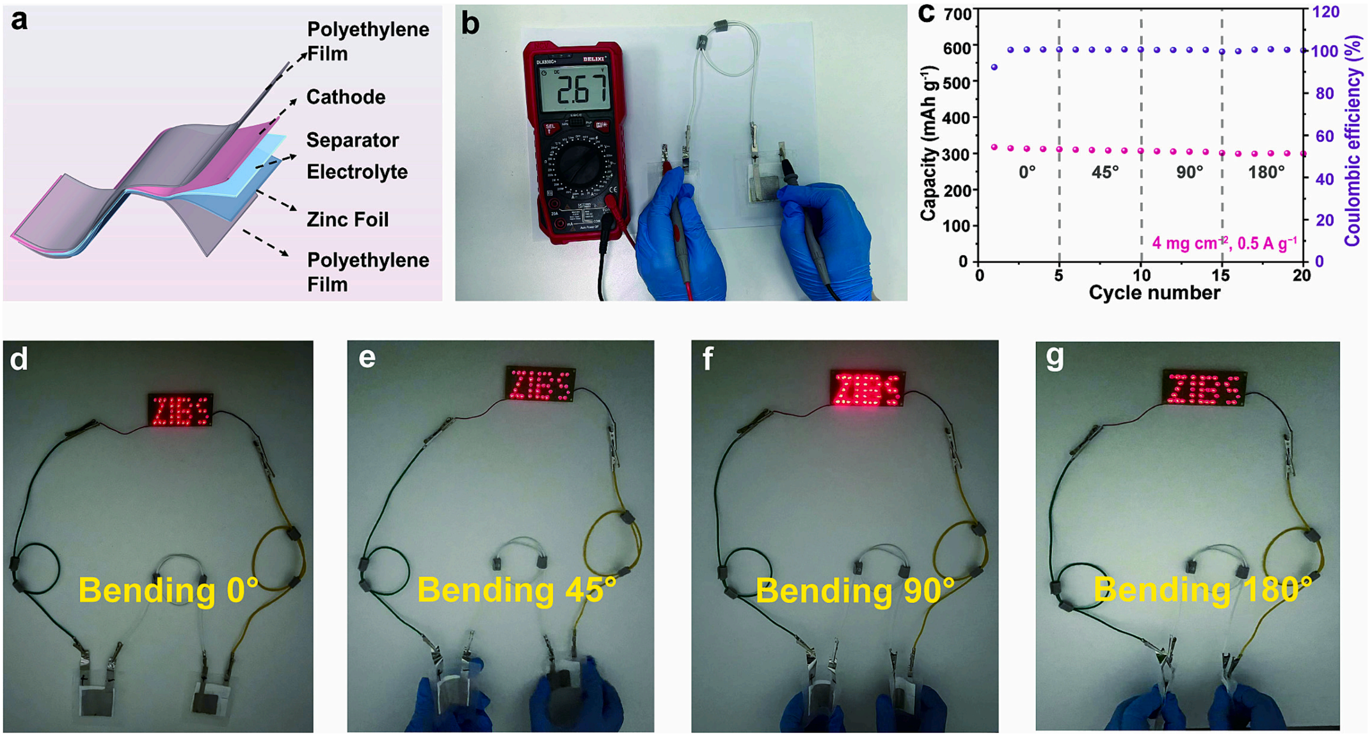

Fig.5. (a) A schematic of an assembled Zn//$CdHVO_y$ pouch cell. (b) Open circuit voltage of two pouch cells connected in series. (c) Cycling stability of the assembled pouch cell under various bending states. (d-g) Digital photographs of LED lights powered by two series-connected pouch cells.

Declaration of competing interest

The authors declare that they have no known competing financial interests or personal relationships that could have appeared to influence the work reported in this paper.

Data availability

Data will be made available on request.

Acknowledgements

This work was finically supported by the National Natural Science Foundation of China (grant number 52101261); the General Program of Natural Science Foundation of Jiangsu Province, China (grant number BK20221179); the China Postdoctoral Science Foundation (grant numbers 2021 M691513 and 2022 T150307); the Postgraduate Research & Practice Innovation Program of Jiangsu Province (KYCX23_3026).

Appendix A. Supplementary data

Supplementary data to this article can be found online at https://doi.org/10.1016/j.cej.2024.156295.

References

[1] D. Chen, X. Rui, Q. Zhang, H. Geng, L. Gan, W. Zhang, C. Li, S. Huang, Y. Yu, Persistent zinc-ion storage in mass-produced V_2O_5 architectures, Nano Energy 60 (2019) 171–178, https://doi.org/10.1016/j.nanoen.2019.03.034.

[2] W. Lv, Z. Shen, X. Li, J. Meng, W. Yang, F. Ding, X. Ju, F. Ye, Y. Li, X. Lyu, M. Wang, Y. Tian, C. Xu, Discovering Cathodic Biocompatibility for Aqueous Zn–MnO_2 Battery: An Integrating Biomass Carbon Strategy, Nano-Micro Lett. 16 (2024) 109, https://doi.org/10.1007/s40820-024-01334-3.

[3] J. Luan, H. Yuan, J. Liu, C. Zhong, Recent advances on charge storage mechanisms and optimization strategies of Mn-based cathode in zinc–manganese oxides batteries, Energy Storage Mater 66 (2024) 103206, https://doi.org/10.1016/j.ensm.2024.103206.

[4] W. Kou, Z. Fang, H. Ding, W. Luo, C. Liu, L. Peng, X. Guo, W. Ding, W. Hou, Valence Engineering Boosts Kinetics and Storage Capacity of Layered Double Hydroxides for Aqueous Magnesium-Ion Batteries, Adv. Funct. Mater. 202406423 (2024), https://doi.org/10.1002/adfm.202406423.

[5] R. Zhao, C. Liu, Y. Zhu, G. Zou, H. Hou, X. Ji, Pathways for MXenes in Solving the Issues of Zinc-Ion Batteries: Achievements and Perspectives, Adv. Funct. Mater. 2316643 (2024), https://doi.org/10.1002/adfm.202316643.

[6] H. Yao, H. Yu, Y. Zheng, N.W. Li, S. Li, D. Luan, X.W. Lou, L. Yu, Pre-intercalation of Ammonium Ions in Layered δ-MnO_2 Nanosheets for High-Performance Aqueous Zinc-Ion Batteries, Angew. Chem. Int. Ed. 62 (2023) e202315257.

[7] X. Jia, C. Liu, Z.G. Neale, J. Yang, G. Cao, Active Materials for Aqueous Zinc Ion Batteries: Synthesis, Crystal Structure, Morphology, and Electrochemistry, Chem. Rev. 120 (2020) 7795–7866, https://doi.org/10.1021/acs.chemrev.9b00628.

[8] A. Zhang, R. Zhao, Y. Wang, J. Yue, J. Yang, X. Wang, C. Wu, Y. Bai, Hybrid Superlattice-Triggered Selective Proton Grotthuss Intercalation in δ-MnO_2 for High-Performance Zinc-Ion Battery, Angew. Chem. Int. Ed. 62 (2023) e202313163.

[9] X. Xiao, Z. Zhang, Y. Wu, J. Xu, X. Gao, R. Xu, W. Huang, Y. Ye, S.T. Oyakhire, P. Zhang, B. Chen, E. Cevik, S.M. Asiri, A. Bozkurt, K. Amine, Y. Cui, Ultrahigh-Loading Manganese-Based Electrodes for Aqueous Batteries via Polymorph Tuning, Adv. Mater. 35 (2023) 2211555, https://doi.org/10.1002/adma.202211555.

[10] Y. Liu, L. Lin, T. Zhang, Z. Xue, J. Liu, D. Chao, X. Sun, A cyano cobalt "electron transfer bridge" boosting the two-electron reaction of a MnO_2 cathode with long lifespan in aqueous zinc batteries, Energy Environ. Sci. 17 (2024) 2521–2529, https://doi.org/10.1039/d3ee03711h.

[11] M. Wu, C. Shi, J. Yang, Y. Zong, Y. Chen, Z. Ren, Y. Zhao, Z. Li, W. Zhang, L. Wang, X. Huang, W. Wen, X. Li, X. Ning, X. Ren, D. Zhu, The LiV_3O_8 Superlattice Cathode with Optimized Zinc Ion Insertion Chemistry for High Mass-Loading Aqueous Zinc-Ion Batteries, Adv. Mater. 36 (2024) 2310434, https://doi.org/10.1002/adma.202310434.

[12] Y. Liu, C. Lu, Y. Yang, W. Chen, F. Ye, H. Dong, Y. Wu, R. Ma, L. Hu, Multiple Cations Nanoconfinement in Ultrathin V_2O_5 Nanosheets Enables Ultrafast Ion Diffusion Kinetics Toward High-performance Zinc Ion Battery, Adv. Mater. 36 (2024) 2312982, https://doi.org/10.1002/adma.202312982.

[13] J. Yang, W. Hou, L. Ye, G. Hou, C. Yan, Y. Zhang, Vanadium Hexacyanoferrate Prussian Blue Analogs for Aqueous Proton Storage: Excellent Electrochemical Properties and Mechanism Insights, Small 20 (2023) 2305386, https://doi.org/10.1002/smll.202305386.

[14] Y. Li, J. Zhao, Q. Hu, T. Hao, H. Cao, X. Huang, Y. Liu, Y. Zhang, D. Lin, Y. Tang, Y. Cai, Prussian blue analogs cathodes for aqueous zinc ion batteries, Mater. Today Energy 29 (2022) 101095, https://doi.org/10.1016/j.mtener.2022.101095.

[15] X. Shi, A. Yi, Q. Liu, Y. Zhang, S. Lin, X. Lu, Nonplanar π-Conjugated Sulfur Heterocyclic Quinone Polymer Cathode for Air-Rechargeable Zinc/Organic Battery with Simultaneously Boosted Output Voltage, Rate Capability, and Cycling Life, ACS Nano 17 (2023) 25005–25013, https://doi.org/10.1021/acsnano.3c07346.

[16] G. He, Y. Liu, D.E. Gray, J. Othon, Conductive polymer composites cathodes for rechargeable aqueous Zn-ion batteries: A mini-review, Compos. Commun. 27 (2021) 100882, https://doi.org/10.1016/j.coco.2021.100882.

[17] M. Chen, S.-C. Zhang, Z.-G. Zou, S.-L. Zhong, W.-Q. Ling, J. Geng, F.-A. Liang, X.-X. Peng, Y. Gao, F.-G. Yu, Review of vanadium-based oxide cathodes as aqueous zinc-ion batteries, Rare Met. 42 (2023) 2868–2905, https://doi.org/10.1007/s12598-023-02303-2.

[18] C. Deng, Y. Li, J. Huang, Building Smarter Aqueous Batteries, Small Methods 8 (2023) 2300832, https://doi.org/10.1002/smtd.202300832.

[19] Y. Guo, H. Jiang, B. Liu, X. Wang, Y. Zhang, J. Sun, J. Wang, Better engineering layered vanadium oxides for aqueous zinc-ion batteries: Going beyond widening the interlayer spacing, SmartMat 5 (2023) e1231.

[20] Y. Liu, J. Huang, X. Li, J. Li, J. Yang, K. Cai, MIL-100(V) derived porous vanadium oxide/carbon microspheres with oxygen defects and intercalated water molecules as high-performance cathode for aqueous zinc ion battery, J. Energy Chem. 90 (2024) 578–589, https://doi.org/10.1016/j.jechem.2023.11.029.

[21] C. Zheng, Z.H. Huang, F.F. Sun, Y. Zhang, H. Li, Y. Liu, T. Ma, Oxygen-Vacancy-Reinforced Vanadium Oxide/Graphene Heterojunction for Accelerated Zinc Storage with Long Life Span, Small 20 (2023) 2306275, https://doi.org/10.1002/smll.202306275.

[22] D.-F. Sun, Z.-J. Wang, T. Tian, X. Yu, D.-D. Yu, X.-Z. Zhou, G.-F. Ma, Z.-Q. Lei, Constructing oxygen deficiency-rich V_2O_3@PEDOT cathode for high-performance aqueous zinc-ion batteries, Rare Met. 43 (2023) 635–646, https://doi.org/10.1007/s12598-023-02434-6.

[23] Y.-H. Zhang, S. Zhang, N. Hu, Y. Liu, J. Ma, P. Han, Z. Hu, X. Wang, G. Cui, Oxygen vacancy chemistry in oxide cathodes, Chem. Soc. Rev. 53 (2024) 3302–3326, https://doi.org/10.1039/d3cs00872j.

[24] Y. Ding, S. Maitra, C. Wang, S. Halder, R. Zheng, T. Barakat, S. Roy, L.H. Chen, B. L. Su, Vacancy defect engineering in semiconductors for solar light-driven environmental remediation and sustainable energy production, Interdiscip. Mater. 1 (2022) 213–255, https://doi.org/10.1002/idm2.12025.

[25] K. Zhang, Q. Zong, K. Ding, Y. Wang, L. Gao, D. Xu, Z. Chen, H. Yu, Cation-driven self-assembly of core–shell covalent organic frameworks@Ti_3CN MXene nanospheres for high-performance aqueous zinc-ion hybrid supercapacitors, Chem. Eng. J. 490 (2024), https://doi.org/10.1016/j.cej.2024.151369.

[26] X. Shi, Y. Sun, Y. Weng, X. Long, T. Lei, J. Zhou, D. Li, J. Zhang, Y. Huang, L. Ci, K. Li, T.-Y. Zhang, Operando chemical strain analysis of CNT/VOOH during zinc insertion in Zn-ion batteries, Energy Environ. Sci. 16 (2023) 4670–4678, https://doi.org/10.1039/d3ee01745a.

[27] F. Wan, Z. Niu, Design Strategies for Vanadium-based Aqueous Zinc-Ion Batteries, Angew. Chem. Int. Ed. 58 (2019) 16358–16367, https://doi.org/10.1002/anie.201903941.

[28] Q. Zong, Y. Zhuang, C. Liu, Q. Kang, Y. Wu, J. Zhang, J. Wang, D. Tao, Q. Zhang, G. Cao, Dual Effects of Metal and Organic Ions Co-Intercalation Boosting the Kinetics and Stability of Hydrated Vanadate Cathodes for Aqueous Zinc-Ion Batteries, Adv. Energy Mater. 13 (2023), https://doi.org/10.1002/aenm.202301480.

[29] L. Shan, Y. Yang, W. Zhang, H. Chen, G. Fang, J. Zhou, S. Liang, Observation of combination displacement/intercalation reaction in aqueous zinc-ion battery, Energy Storage Mater 18 (2019) 10–14, https://doi.org/10.1016/j.ensm.2018.08.008.

[30] X. Guan, Q. Sun, C. Sun, T. Duan, W. Nie, Y. Liu, K. Zhao, H. Cheng, X. Lu, Tremella-like Hydrated Vanadium Oxide Cathode with an Architectural Design Strategy toward Ultralong Lifespan Aqueous Zinc-Ion Batteries, ACS Appl. Mater. Interfaces 13 (2021) 41688–41697, https://doi.org/10.1021/acsami.1c11560.

[31] S. Luo, X. Cao, Q. Su, Y. Zhang, S. Liu, X. Xie, S. Liang, A. Pan, Layered Barium Vanadate Cathodes for Aqueous Zinc Batteries: Enhancing Cycling Stability through Inhibition of Vanadium Dissolution, ACS Appl. Energy Mater. 4 (2021) 6197–6204, https://doi.org/10.1021/acsaem.1c00979.

[32] W. Zhou, M. Chen, A. Wang, A. Huang, J. Chen, X. Xu, C.-P. Wong, Optimizing the electrolyte salt of aqueous zinc-ion batteries based on a high-performance calcium vanadate hydrate cathode material, J. Energy Chem. 52 (2021) 377–384, https://doi.org/10.1016/j.jechem.2020.05.005.

[33] Y. Li, W. Yang, W. Yang, Y. Huang, G. Wang, C. Xu, F. Kang, L. Dong, High-performance zinc-ion batteries enabled by electrochemically induced transformation of vanadium oxide cathodes, J. Energy Chem. 60 (2021) 233–240, https://doi.org/10.1016/j.jechem.2021.01.025.

[34] W. Deng, C. Li, W. Zou, Y. Xu, Y. Chen, R. Li, Understanding the Super-Theoretical Capacity Behavior of VO_2 in Aqueous Zn Batteries, Small 20 (2023) 2309527, https://doi.org/10.1002/smll.202309527.

[35] X. Wang, Z. Zhang, M. Huang, J. Feng, S. Xiong, B. Xi, In Situ Electrochemically Activated Vanadium Oxide Cathode for Advanced Aqueous Zn-Ion Batteries, Nano Lett. 22 (2021) 119–127, https://doi.org/10.1021/acs.nanolett.1c03409.

[36] Y. Liu, C. Gao, Y. Sun, X. Hao, Z. Pi, M. Yang, X. Zhao, K. Cai, Enhancing the electrochemical activation kinetics of V_2O_3 for high-performance aqueous zinc-ion battery cathode materials, Chem. Eng. J. 490 (2024) 151535, https://doi.org/10.1016/j.cej.2024.151535.

[37] Y. Liu, J. Zhang, Y. Liu, M. Zhang, Z. Pan, K. Cai, Controllable Design of Metal-Organic Framework-Derived Vanadium Oxynitride for High-Capacity and Long-Cycle Aqueous Zn-Ion Batteries, Small 2401922 (2024), https://doi.org/10.1002/smll.202401922.

[38] J. Hu, Y. Xie, J. Zheng, H. Li, T. Wang, Y. Lai, Z. Zhang, Encapsulating V_2O_3 Nanoparticles in Hierarchical Porous Carbon Nanosheets via C-O–V Bonds for Fast and Durable Potassium-Ion Storage, ACS Appl. Mater. Interfaces 13 (2021) 12149–12158, https://doi.org/10.1021/acsami.1c01303.

[39] P. Shvets, O. Dikaya, K. Maksimova, A. Goikhman, A review of Raman spectroscopy of vanadium oxides, J. Raman Spectrosc. 50 (2019) 1226–1244, https://doi.org/10.1002/jrs.5616.

[40] C. Fan, B. Zhu, X. Zhang, C. Bi, D. Zhang, Z. Zong, Y. Fan, Highly Stable Acid-Induced Emission-Enhancing Cd-MOFs: Synthesis, Characterization, and Detection of Glutamic Acid in Water and Fe Ions in Acid, Inorg. Chem. 60 (2021) 6339–6348, https://doi.org/10.1021/acs.inorgchem.1c00017.

[41] X. Liu, Z. Wang, Y. Niu, C. Liu, H. Chen, X. Ren, Z. Liu, W.-M. Lau, D. Zhou, Electrospun V_2O_3@Carbon Nanofibers as a Flexible and Binder-Free Cathode for Highly Stable Aqueous Zn-Ion Full Batteries, ACS Appl. Energy Mater. 5 (2022) 3525–3535, https://doi.org/10.1021/acsaem.1c04068.

[42] V. Mounasamy, G.K. Mani, D. Ponnusamy, K. Tsuchiya, P.R. Reshma, A.K. Prasad, S. Madanagurusamy, Cadmium metavanadate mixed oxide nanorods for the chemiresistive detection of methane molecules, New J. Chem. 44 (2020) 12473–12485, https://doi.org/10.1039/d0nj02690e.

[43] Y. Du, X. Wang, J. Sun, Tunable oxygen vacancy concentration in vanadium oxide as mass-produced cathode for aqueous zinc-ion batteries, Nano Res. 14 (2020) 754–761, https://doi.org/10.1007/s12274-020-3109-x.

[44] L. Chen, Z. Yang, F. Cui, J. Meng, H. Chen, X. Zeng, Enhanced rate and cycling performances of hollow V_2O_5 nanospheres for aqueous zinc ion battery cathode, Appl. Surf. Sci. 507 (2020) 145137, https://doi.org/10.1016/j.apsusc.2019.145137.

[45] W. He, Z. Fan, Z. Huang, X. Liu, J. Qian, M. Ni, P. Zhang, L. Hu, Z. Sun, A Li^+ and PANI co-intercalation strategy for hydrated V_2O_5 to enhance zinc ion storage performance, J. Mater. Chem. A 10 (2022) 18962–18971, https://doi.org/10.1039/d2ta03145k.

[46] Y. Qi, J. Huang, L. Yan, Y. Cao, J. Xu, D. Bin, M. Liao, Y. Xia, Towards high-performance aqueous zinc-ion battery via cesium ion intercalated vanadium oxide nanorods, Chem. Eng. J. 442 (2022) 136349, https://doi.org/10.1016/j.cej.2022.136349.

[47] Y. Liu, Y. Sun, J. Zhang, X. Hao, M. Zhang, P. Wei, X. Zhao, K. Cai, Electrochemically inducing $V_2O_5{\cdot}nH_2O$ nanoarrays vertically growth on VSx microrods for highly stable zinc ion battery cathode, Nano Energy 120 (2024) 109152, https://doi.org/10.1016/j.nanoen.2023.109152.

[48] N. Liu, X. Wu, L. Fan, S. Gong, Z. Guo, A. Chen, C. Zhao, Y. Mao, N. Zhang, K. Sun, Intercalation Pseudocapacitive Zn^{2+} Storage with Hydrated Vanadium Dioxide toward Ultrahigh Rate Performance, Adv. Mater. 32 (2020) 1908420, https://doi.org/10.1002/adma.201908420.

[49] X. Xie, G. Fang, W. Xu, J. Li, M. Long, S. Liang, G. Cao, A. Pan, In Situ Defect Induction in Close-Packed Lattice Plane for the Efficient Zinc Ion Storage, Small 17 (2021) 2101944, https://doi.org/10.1002/smll.202101944.

[50] X. Wang, B. Xi, X. Ma, Z. Feng, Y. Jia, J. Feng, Y. Qian, S. Xiong, Boosting Zinc-Ion Storage Capability by Effectively Suppressing Vanadium Dissolution Based on Robust Layered Barium Vanadate, Nano Lett. 20 (2020) 2899–2906, https://doi.org/10.1021/acs.nanolett.0c00732.

[51] B. Sambandam, V. Soundharrajan, S. Kim, M.H. Alfaruqi, J. Jo, S. Kim, V. Mathew, Y.-K. Sun, J. Kim, $K_2V_6O_{16}{\cdot}2.7H_2O$ nanorod cathode: an advanced intercalation system for high energy aqueous rechargeable Zn-ion batteries, J. Mater. Chem. A 6 (2018) 15530–15539, https://doi.org/10.1039/c8ta02018c.

[52] Y. Luo, L. Wei, H. Geng, Y. Zhang, Y. Yang, C.C. Li, Amorphous Bimetallic Oxides Fe–V–O with Tunable Compositions toward Rechargeable Zn-Ion Batteries with Excellent Low-Temperature Performance, ACS Appl. Mater. Interfaces 12 (2020) 11753–11760, https://doi.org/10.1021/acsami.0c00057.

[53] M. Ghosh, S. Dilwale, V. Vijayakumar, S. Kurungot, Scalable Synthesis of Manganese-Doped Hydrated Vanadium Oxide as a Cathode Material for Aqueous Zinc-Metal Battery, ACS Appl. Mater. Interfaces 12 (2020) 48542–48552, https://doi.org/10.1021/acsami.0c13221.

[54] Y. Ding, Y. Peng, W. Chen, Y. Niu, S. Wu, X. Zhang, L. Hu, V-MOF derived porous V_2O_5 nanoplates for high performance aqueous zinc ion battery, Appl. Surf. Sci. 493 (2019) 368–374, https://doi.org/10.1016/j.apsusc.2019.07.026.

[55] Y. Ding, Y. Peng, S. Chen, X. Zhang, Z. Li, L. Zhu, L.-E. Mo, L. Hu, Hierarchical Porous Metallic V_2O_3@C for Advanced Aqueous Zinc-Ion Batteries, ACS Appl. Mater. Interfaces 11 (2019) 44109–44117, https://doi.org/10.1021/acsami.9b13729.

[56] W. Chen, J. Gu, Q. Liu, M. Yang, C. Zhan, X. Zang, T.A. Pham, G. Liu, W. Zhang, D. Zhang, B. Dunn, Y. Morris Wang, Two-dimensional quantum-sheet films with sub-1.2 nm channels for ultrahigh-rate electrochemical capacitance, Nat. Nanotechnol. 17 (2021) 153–158, https://doi.org/10.1038/s41565-021-01020-0.